RESEARCH ARTICLE

NANO · MICRO small
www.small-journal.com

Rapid Synthesis of Ruthenium–Copper Nanocomposites as High-Performance Bifunctional Electrocatalysts for Electrochemical Water Splitting

*Dingjie Pan, Qiming Liu, Bingzhe Yu, Davida Briana DuBois, John Tressel, Sarah Yu, Noah Kaleekal, Sophia Trabanino, Yillin Jeon, Frank Bridges, and Shaowei Chen**

Development of high-performance, low-cost catalysts for electrochemical water splitting is key to sustainable hydrogen production. Herein, ultrafast synthesis of carbon-supported ruthenium–copper (RuCu/C) nanocomposites is reported by magnetic induction heating, where the rapid Joule's heating of $RuCl_3$ and $CuCl_2$ at 200 A for 10 s produces Ru–Cl residues-decorated Ru nanocrystals dispersed on a $CuCl_x$ scaffold, featuring effective Ru to Cu charge transfer. Among the series, the RuCu/C-3 sample exhibits the best activity in 1 M KOH toward both the hydrogen evolution reaction (HER) and oxygen evolution reaction (OER), with an overpotential of only −23 and +270 mV to reach 10 mA cm^{-2}, respectively. When RuCu/C-3 is used as bifunctional catalysts for electrochemical water splitting, a low cell voltage of 1.53 V is needed to produce 10 mA cm^{-2}, markedly better than that with a mixture of commercial Pt/C+RuO_2 (1.59 V). In situ X-ray absorption spectroscopy measurements show that the bifunctional activity is due to reduction of the Ru–Cl residues at low electrode potentials that enriches metallic Ru and oxidation at high electrode potentials that facilitates the formation of amorphous RuO_x. These findings highlight the unique potential of MIH in the ultrafast synthesis of high-performance catalysts for electrochemical water splitting.

1. Introduction

Hydrogen has emerged as a pivotal energy source to continuously fulfill the energy demands for human consumption while striving for zero carbon emissions.[1–2] At present, hydrogen production relies predominantly on natural gas through steam methane reforming, which is deemed unsustainable.[3] The synthesis of hydrogen through water splitting using renewable electricity is imperative to transition from conventional (grey) hydrogen to environmentally friendly (green) hydrogen.[4] In the electrochemical water splitting process, two half-reactions are involved: hydrogen evolution reaction (HER) at the cathode and oxygen evolution reaction (OER) at the anode. Notably, both half-reactions necessitate the development of effective catalysts to boost the electron-transfer kinetics, such that a sufficiently high current density can be produced for practical applications. Currently, commercial catalysts are based on precious metals. For instance, carbon-supported platinum nanoparticles (Pt/C) are the commercial benchmark for HER, whereas RuO_2 and IrO_2 for OER. Notably, these catalysts are active toward either HER or OER only. It will be of fundamental significance to develop bifunctional electrocatalysts toward both half-reactions to streamline device fabrication and integration and further advance the technology.[5–9] One effective strategy is the deliberate integration of various functional components that are respectively active toward HER and OER into a heterogeneous composite structure, as demonstrated in a series of recent studies.[10–14]

Among these, ruthenium-based nanocomposites have garnered considerable attention. First of all, ruthenium nanoparticles and single atoms have been known to exhibit excellent electrocatalytic activity toward HER with a markedly reduced cost, as compared to platinum (Pt), making it a viable substitute for Pt-based commercial benchmarks.[15–16] This is primarily ascribed to an optimal bond strength with hydrogen (≈65 kcal mol^{-1}) that is close to that of Pt.[17] In fact, according to the HER volcano plot, the Gibbs free energy of hydrogen adsorption (ΔG_H) is close to 0 eV for both Pt and Ru.[18–20] Ru-based nanocomposites have also been found to exhibit unique electrocatalytic activity toward OER (in fact, RuO_2 is a commercial benchmark for OER). In a recent study, Wang and coworkers[21] prepared graphene composites with Ru-RuO_2 heterostructures via calcination of $RuCl_3$, thiourea, and N,P-codoped reduced graphene oxide nanosheets. The resulting Ru-RuO_2@NPC nanocomposites exhibited remarkable bifunctional activity toward both HER and OER within a wide

D. Pan, Q. Liu, B. Yu, D. B. DuBois, J. Tressel, S. Yu, N. Kaleekal, S. Trabanino, Y. Jeon, S. Chen
Department of Chemistry of Biochemistry
University of California
1156 High Street, Santa Cruz, CA 95064, USA
E-mail: shaowei@ucsc.edu

F. Bridges
Department of Physics
University of California
1156 High Street, Santa Cruz, CA 95064, USA

The ORCID identification number(s) for the author(s) of this article can be found under https://doi.org/10.1002/smll.202404729

DOI: 10.1002/smll.202404729

range of pH, and a low cell voltage of 1.46 V was needed to reach the current density of 10 mA cm^{-2} in electrochemical water splitting. This was ascribed to charge transfer at the Ru-RuO_2 Mott–Schottky junctions that shifted the *d*-band center at the interface to the intermediate between those of Ru and RuO_2 and facilitated the adsorption and desorption of key reaction intermediates (e.g., $^*H$, $^*O$, $^*OH$, and $^*OOH$). In another study, You and coworkers[22] prepared Ru-G/CC nanocomposites where Ru nanoparticles with a mix of amorphous/crystalline structures were grown on carbon cloth (CC) via a glycerol-assisted synthesis. The optimal Ru-G/CC exhibited a low overpotential ($\eta_{HER,10}$) of −40 mV to reach the current density of 10 mA cm^{-2} and a Tafel slope of 76 mV dec^{-1} for HER, as well as a low overpotential ($\eta_{OER,10}$) of +270 mV and Tafel slope of 63 mV dec^{-1} for OER. Density functional theory (DFT) calculations showed that the mixture of the amorphous and crystalline Ru characters led to a reduced energy barrier in HER, while the in situ electrochemically produced Ru/RuO_2 species was conducive to OER. In another study, Jiang and coworkers[23] prepared Ru@RuO_2 core-shell nanorods by thermal treatment of Ru nanorods in air at controlled temperatures, and observed an excellent bifunctional catalytic performance, where the HER activity ($\eta_{HER,10}$ = −137 mV) was comparable to that of 40% Pt/C while the OER activity ($\eta_{OER,10}$ = +320 mV) was 6.5 times higher than that of IrO_2.

In these prior studies, the Ru-based catalysts were prepared mostly via conventional pyrolysis and wet chemistry methods, which are time-consuming and energy-intensive.[24] Such issues can be mitigated by ultrafast synthesis based on, for instance, magnetic induction heating (MIH), where the rapid heating and cooling makes it possible to produce samples within seconds, and more importantly, to facilitate the formation of nonequilibrium/metastable structures that are unattainable in conventional heating methods.[25] In MIH, the Joule effect results in an ultrafast heating rate (e.g., 200 °C s^{-1}) reaching a temperature over 1000 °C within seconds, in contrast to conventional methods based on tube furnaces and hydrothermal processes that exhibit much slower heating (<10 °C min^{-1}). This has indeed been demonstrated in several recent studies in the preparation of a variety of functional nanocomposites that exhibited unprecedented electrocatalytic activity toward HER and OER, e.g., FeNi spinel oxides with a good mixing of the Fe and Ni phases,[26] defective carbon-encapsulated Co nanoparticle composites,[27] Ru nanoparticles with Ru–Cl residues,[28] and amorphous MoS_x composites.[29]

In these studies, the induction current and heating time played a critical role in controlling the heating temperature and ultimately the materials structure and performance. For instance, in the MIH preparation of ruthenium/carbon (Ru/C) nanocomposites using $RuCl_3$ and carbon black as the precursors,[28] the sample prepared at 200 A for 10 s consisted mostly of amorphous Ru clusters due to the relatively low heating temperature and hence incomplete decomposition of $RuCl_3$, whereas with the induction current increased to 300 A, Ru nanocrystals started to emerge in the sample and were decorated with abundant Ru–Cl residues. At higher induction currents (400–600 A), agglomerates of Ru nanocrystals became the dominant components with a marked diminishment of the Ru–Cl residues. Among the sample series, the sample prepared at 300 A exhibited the best HER activity in both acidic ($\eta_{HER,10}$ = −23 mV) and alkaline media ($\eta_{HER,10}$ = −12 mV), which was ascribed to the Ru–Cl anion residues that regulated the electron density of Ru and the interaction with H intermediates. That is, the remarkable HER performance was ascribed to the synergistic interactions between crystalline Ru and anion residues. Yet the sample was mostly inactive toward OER.

In the present study, we demonstrated that with the addition of a second metal precursor, $CuCl_2$, MIH treatment of $RuCl_3$ at 200 A led to the production of RuCu/C nanocomposites which consisted of Ru–Cl enriched Ru nanocrystals supported on a $CuCl_x$ scaffold, exhibited a remarkable activity toward both HER and OER and could be used as bifunctional catalysts for electrochemical water splitting. The enhanced crystallinity of the ruthenium nanoparticles, as compared to that in the absence of $CuCl_2$,[28] was facilitated likely by charge transfer from the Cu(I) species derived from (partial) thermal decomposition of $CuCl_2$. Among the series, the RuCu/C-3 sample, with a Ru:Cu atomic ratio of ≈4:1, exhibited the best bifunctional activities for both HER and OER, with an $\eta_{HER,10}$ of −23 mV and $\eta_{OER,10}$ of +270 mV in 1 M KOH. In situ X-ray absorption spectroscopy (XAS) measurements showed that at low electrode potentials, electroreduction of the Ru–Cl residues facilitated the enrichment of (metallic) Ru nanoparticles that were responsible for the HER activity, whereas at high electrode potentials, oxidation of the Ru–Cl residues led to the formation of amorphous RuO_x that was active toward OER. Indeed, by using RuCu/C-3 as the dual catalysts for full water splitting, a low cell voltage of 1.53 V was needed to reach the current density of 10 mA cm^{-2}, a performance markedly better than that (1.59 V) with a mixture of commercial Pt/C and RuO_2. It should be noted that the obtained RuCu/C nanocomposites were markedly different from the ruthenium–copper alloys that were reported previously via conventional synthesis methods, where the metallic state led to electrocatalytic activity toward only HER but not OER.[30–33]

2. Results and Discussion

2.1. Sample Synthesis and Structural Characterization

The RuCu/C nanocomposites were synthesized using the MIH setup in **Scheme 1**. Experimentally, *x* mL of 0.1 M $RuCl_3$ and *y* mL of 0.1 M $CuCl_2$ solutions (with *x* + y = 1 mL, i.e., a total metal feed of 0.1 mmol) were mixed with 40 mg of carbon black. After freeze-drying of the mixture overnight, the obtained black powders were subject to MIH treatment at the induction current of 200 A for 10 s.[27] Four samples were prepared, RuCu/C-1, RuCu/C-2, RuCu/C-3, and RuCu/C-4 in the order of increasing feed ratio of $RuCl_3$ versus $CuCl_2$ at *x*:y = 1:4, 1:2, 2:1, and 4:1, respectively. For comparison, monometallic Ru/C and Cu/C samples were synthesized in the same manner but with only the $RuCl_3$ or $CuCl_2$ precursor. The synthetic details are included in the Experimental Section.

The sample structures were first examined by transmission electron microscopy (TEM) measurements. From **Figure 1a**, one can see that the RuCu/C-3 sample consisted of a number of (dark-contrast) nanoparticles deposited onto (low-contrast) carbon black particle surfaces. Statistical analysis based on over 100 nanoparticles showed that the nanoparticles mostly fell within the range of 3–10 nm, with an average diameter of 5.27 ± 2.72 nm, as depicted in the core size histogram (Figure 1a inset).

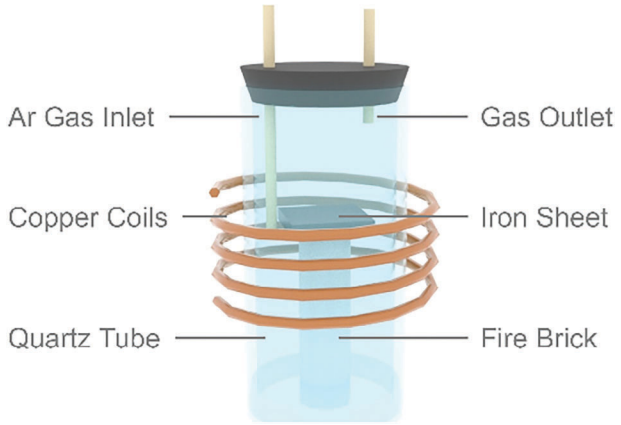

Scheme 1. Schematic illustration of the MIH setup for rapid synthesis of the RuCu/C nanocomposites.

In high-resolution TEM measurements (Figure 1b) the nanoparticles can be seen to possess well-defined lattice fringes, with an interplanar spacing of 0.216 and 0.232 nm that can be assigned to the (002) and (100) crystal planes of *hcp* Ru, respectively,[34–36] indicating the formation of metallic Ru nanoparticles. Consistent results were obtained in energy-dispersive X-ray spectroscopy (EDS)-based elemental mapping analysis (Figure 1c), where Ru can be seen to be enriched in the nanoparticles that are scattered onto the carbon scaffold (Figure S1, Supporting Information). Notably, the elements of Cu, Cl, and O can also be clearly resolved within the sample, and Cl and O exhibit a clear overlap with Ru. This suggests that the sample likely consisted of Ru nanoparticles enriched with metal-Cl/O residues and the nanoparticles were dispersed onto a copper-Cl/O matrix.[28] A similar morphology was observed with Ru/C and other RuCu/C samples in the series (Figures S2–S5, Supporting Information).

Note that for the Cu/C sample, no nanoparticles can be found and the sample was largely amorphous (Figure S6, Supporting Information), suggesting incomplete decomposition of $CuCl_2$, due to the relatively low MIH current (200 A) and short heating time (10 s), which corresponded to a temperature of ≈600 °C. In fact, in a previous study based on thermogravimetric analysis (TGA),[37] it has been shown that the thermal decomposition of $CuCl_2$ commenced at ≈400 °C producing CuCl. For the Ru/C sample (Figure S5, Supporting Information), whereas $RuCl_3$ can be thermally decomposed to Ru(0) at a lower temperature of ≈350 °C,[38] the ultrafast MIH process resulted in the formation of largely non-crystalline nanoparticles, consistent with results observed previously.[28] By contrast, well-defined lattice fringes were observed with the RuCu/C sample series (Figures S2–S4, Supporting Information). This is plausibly due to the markedly lower $Cu^{+2/+1}$ reduction potential (+0.153 V) as compared to that of $Ru^{+3/0}$ (+0.68 V),[39] such that galvanic charge transfer from Cu(I) to Ru facilitated the formation of nanocrystalline Ru. Such synergistic interactions between the copper and ruthenium precursors likely led to the slight variation of the Ru nanoparticle core size among the sample series. As shown in Figure S7 (Supporting Information), in comparison to Ru/C which exhibited an average particle core size of 2.88 ± 2.38 nm, the addition of $CuCl_2$ in sample synthesis produced markedly larger nanoparticles in RuCu/C-4 (3.88 ± 2.67 nm) and RuCu/C-3 (5.27 ± 2.72 nm); yet a further increase of $CuCl_2$ feed (and concurrently a reduced feed of $RuCl_3$) produced only smaller-sized nanoparticles, 2.45 ± 1.22 nm for RuCu/C-2, and 1.57 ± 0.63 nm for RuCu/C-1, likely due to a diminished supply of Ru for nanoparticle growth.

Further structural analysis was carried out in X-ray diffraction (XRD) measurements. From Figure S8 (Supporting Information), one can see that all samples exhibited a broad peak at $2\theta \approx 24°$ that can be assigned to the (002) planes of the carbon black scaffold.[40–41] For the Cu/C sample, three additional diffraction peaks appeared at $2\theta = 16.26°$, 32.42°, and 37.48°, slightly larger than those anticipated for the (001), (20-2), and (111) planes of pristine $CuCl_2$,[42] respectively, suggesting reduced lattice spacings likely as a result of partial decomposition of $CuCl_2$ by MIH. Notably, these diffraction peaks diminished markedly in intensity in the RuCu/C samples with the increasing feed of $RuCl_3$ (and decreasing feed of $CuCl_2$), where the Ru(100), (002), and (101) diffractions emerged at 38.4°, 42.14°, and 43.88°, respectively, and the RuCu/C-3 sample exhibited the sharpest peaks, consistent with results from TEM measurements.[43]

The elemental compositions and valencies of the samples were then examined by X-ray photoelectron spectroscopy (XPS) measurements. From the survey spectra in Figure S9a (Supporting Information), the Cl 2p, C 1s, Ru 3p, O 1s, and Cu 2p electrons can be readily resolved at ≈198, 284, 464, 531, and 935 eV, respectively, for all RuCu/C samples. A similar profile was observed with Ru/C and Cu/C, except for the Cu and Ru signals, respectively. Based on the integrated peak areas, the Ru (Cu) contents can be seen to increase (decrease) with increasing Ru:Cu feed ratio (Table S1, Supporting Information), in qualitative agreement with results from inductively coupled plasma-optical emission spectrometry (ICP-OES) measurements (Table S2, Supporting Information), where the Ru:Cu atomic ratio increased in the order of RuCu/C-1 (0.43) < RuCu/C-2 (0.56) < RuCu/C-3 (4.08) < RuCu/C-4 (6.04). One may note that these values are appreciably higher than the initial feed ratios, likely because of the greater thermal volatility of $CuCl_2$ as compared to $RuCl_3$.[37–38]

The high-resolution scans of the Ru 3p electrons are shown in **Figure 2**a, where two doublets can be deconvoluted for the RuCu/C and Ru/C samples. For Ru/C, the doublet (green curves) at 462.71/484.91 eV can be ascribed to the $3p_{3/2}/3p_{1/2}$ electrons of metallic Ru, consistent with the formation of Ru nanoparticles;[28,44–47] whereas the other one (blue curves) at 464.33/486.53 eV are consistent with those of $Ru^{\delta+}$ species.[44,48] Upon the loading of $CuCl_2$ in sample synthesis, these binding energies increased by 0.5–1.5 eV with an increasing Cu feed from RuCu/C-4 to RuCu/C-1 (Table S3, Supporting Information), suggesting the formation of increasingly electron-deficient Ru sites. Nevertheless, one can see that the fraction of $Ru^{\delta+}$ species remained rather consistent at roughly 50% of the total Ru content among the sample series (Table S4, Supporting Information), most likely as a result of the ultrafast synthesis of MIH. The Cu 2p spectra are shown in Figure 2b. Deconvolution yielded a doublet (red curves) at 934.41/954.06 eV for Cu/C that can be ascribed to the Cu(II) $2p_{3/2}/2p_{1/2}$ electrons (three corresponding satellite peaks can be resolved at 940.81, 943.66, and 962.15 eV).[49–50] The RuCu/C samples exhibited a similar profile but the doublet shifted to lower energies (Table S3, Supporting Information), RuCu/C-3 (932.90/953.59 eV) < RuCu/C-4 (933.12/952.47 eV) <

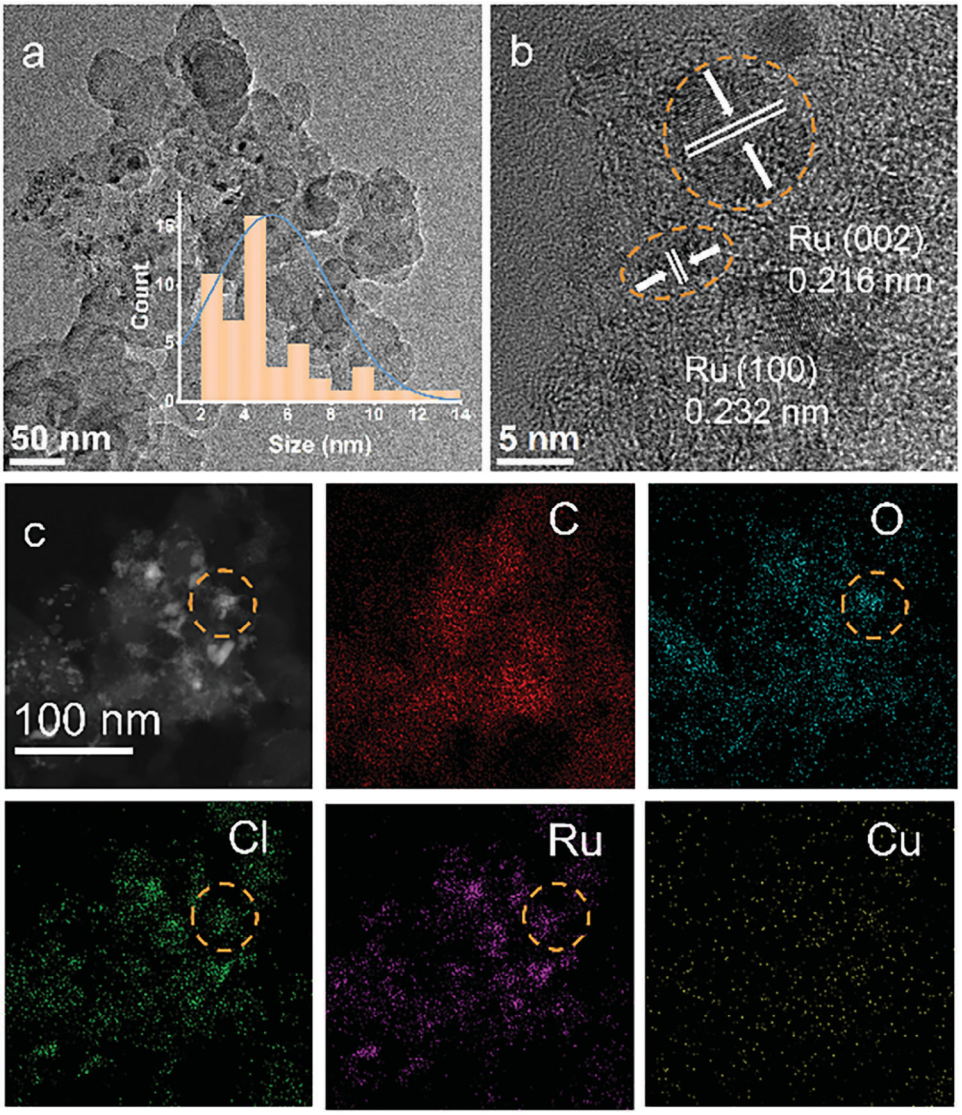

Figure 1. a,b) TEM image of the RuCu/C-3 sample with the corresponding size histogram shown in the inset on the lower-right of (a), and c) the corresponding elemental maps.

RuCu/C-2 (933.78/953.13 eV) < RuCu/C-1 (933.85/953.20 eV) < Cu/C (934.41/954.06 eV). The absence of metallic Cu in the sample series is consistent with the incomplete decomposition of $CuCl_2$.[49] This is further confirmed by results from the Cu LMM spectra (Figure S9b, Supporting Information).[51–52]

Figure 2c shows the O 1s spectra, where all samples can be seen to consist of two species, C═O (blue curve) at 531.43 eV and C—O (green curve) at 533.21 eV.[44,53] The fact that no O 1s peak can be resolved below 530 eV indicates the absence of metal-O in metal oxides and that the ionic Ru and Cu species were most likely involved in the formation of metal-Cl residues. Indeed, from the Cl 2p spectra in Figure 2d, two doublets can be resolved, and the major one (blue curves) at 197.86/199.49 eV can be ascribed to the $2p_{3/2}/2p_{1/2}$ electrons of metal-Cl, confirming the formation of heteroanion residues in the samples, in good agreement with results from the above EDS elemental mapping analysis, whereas the minor one (green curves) at 199.71/201.41 eV are due to organic Cl.[54–55] In addition, for the Ru/C sample, the atomic ratio of Ru to Cl in Ru–Cl was estimated to be 1:2.11; and the Cu:Cl ratio in Cu–Cl was determined to be 1:1.37 for Cu/C, both clearly lower than those of their respective precursors of $RuCl_3$ and $CuCl_2$ (Figure S10, Table S1–S4, Supporting Information). Assuming that such stoichiometric ratios were retained in the RuCu/C sample series, based on the ionic Ru and Cu contents (Table S4, Supporting Information), the content of meta-Cl can be estimated to be 0.90 at% for RuCu/C-1, 1.12 at% for RuCu/C-2, 1.02 at% for RuCu/C-3, and 2.08 at% for RuCu/C-4, which were indeed very close to the experimental values of 1.07, 1.09, 1.33, and 2.87 at%. Taken together, these results suggest that the samples consisted of Ru nanoparticles decorated with Ru/Cu–Cl residues due to the rapid heating of MIH.[28]

The corresponding C 1s spectra are shown in Figure S9c (Supporting Information). The C═C (red peak) and C—C (blue peak) species can be identified at 284.32 and 285.00 eV for Cu/C,[56]

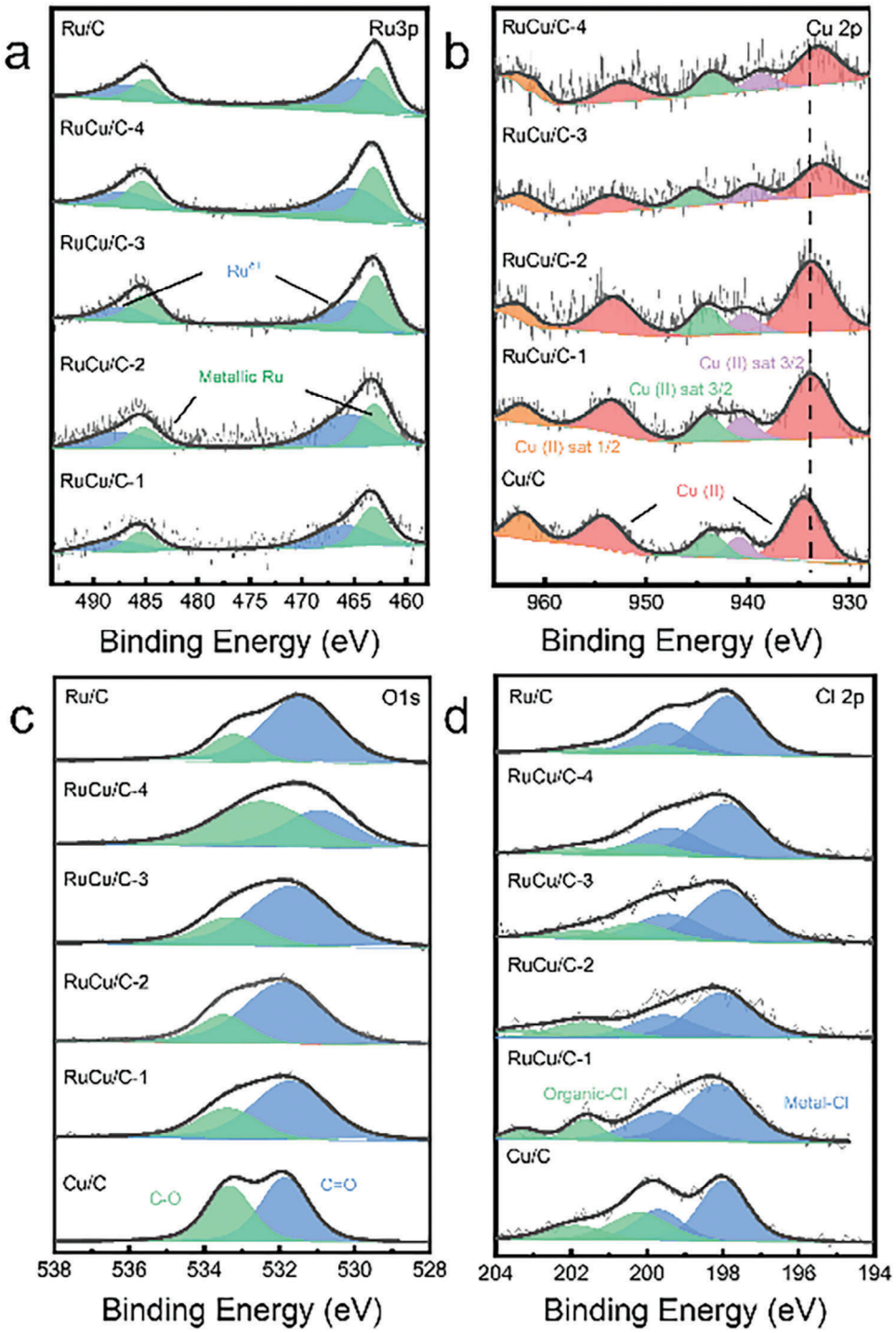

Figure 2. High-resolution XPS spectra of the a) Ru 3p electrons of RuCu/C-1, RuCu/C-2, RuCu/C-3, RuCu/C-4, and Ru/C; b) Cu 2p electrons of Cu/C, RuCu/C-1, RuCu/C-2, RuCu/C-3, and RuCu/C-4; c) O 1s and d) Cl 2p electrons of Cu/C, RuCu/C-1, RuCu/C-2, RuCu/C-3, RuCu/C-4, and Ru/C. Grey curves are experimental data and colored peaks are deconvolution fits.

respectively, and shifted to a slightly lower binding energy with the increasing loading of Ru (Table S3, Supporting Information). This electron enrichment of the Vulcan carbon support is likely due to charge redistribution with the deposition of Ru nanoparticles onto the carbon scaffold. The Ru 3d peaks can also be resolved in RuCu/C-3, RuCu/C-4, and RuCu/C-5 but not in RuCu/C-1 and RuCu/C-2, likely due to a low Ru content in the latter.

Further structural insights were obtained from XAS measurements. **Figure** 3a,b shows the Ru K-edge X-ray absorption

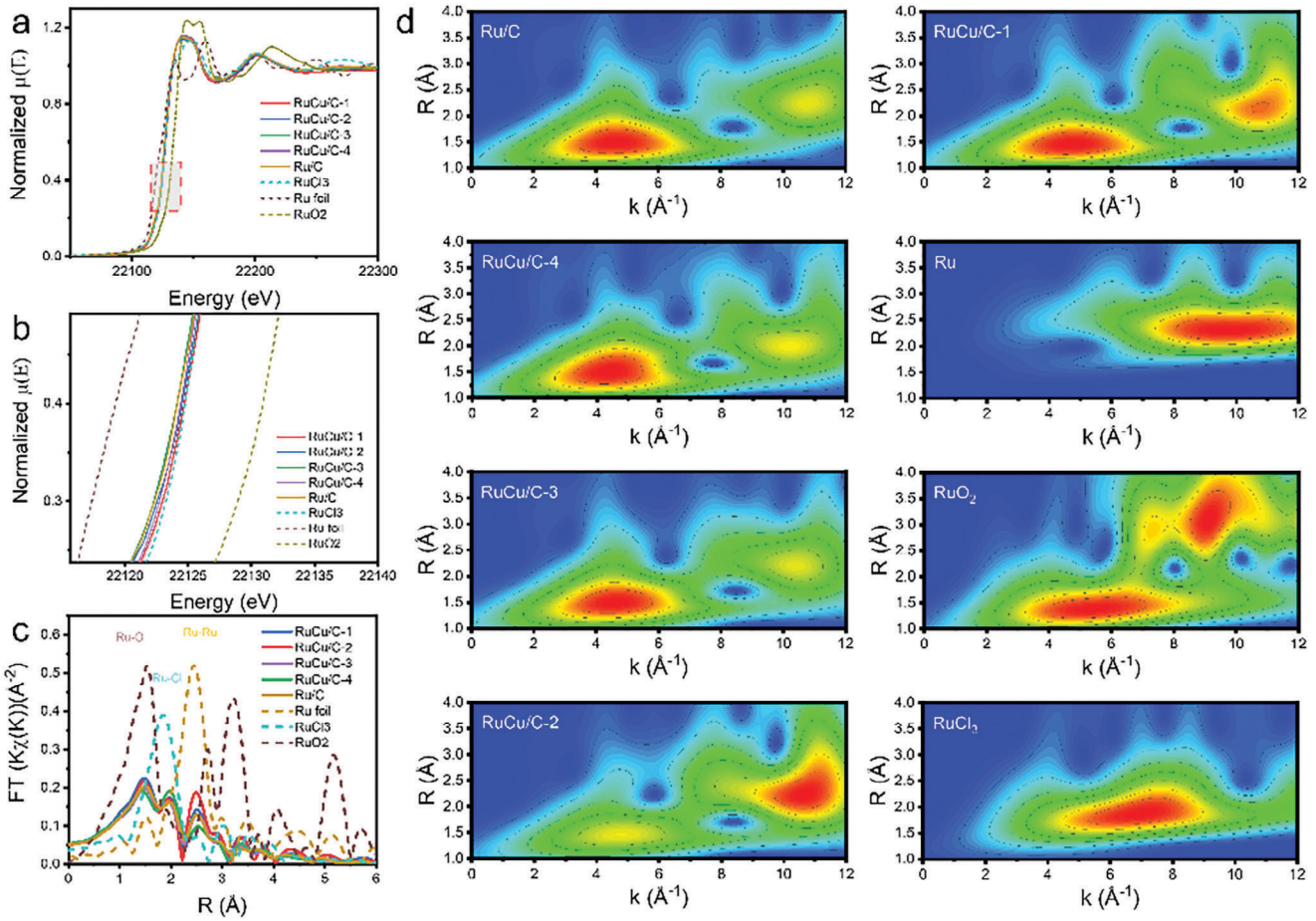

Figure 3. a) X-ray absorption near-edge spectra (XANES), b) zoom-in of the red box in panel (a), c) the corresponding Fourier transformed extended X-ray absorption spectra (FT-EXAFS) of RuCu/C-4, RuCu/C-3, RuCu/C-2, RuCu/C-1, and Ru/C, and d) EXAFS wavelet transform analysis ($\kappa = 5$, $\sigma = 1$).

near-edge spectra (XANES) of the Ru/C and RuCu/C sample series, along with Ru foil, RuO_2, and $RuCl_3$ references. One can see that the absorption edges were all located between those of Ru foil and RuO_2 and close to that of the $RuCl_3$ reference, indicating that the average valence state was close to +3. In fact, from the zoom-in of the absorption edge (Figure 3b) the absorption edge energy can be seen to decrease slightly in the order of $RuCl_3$ > RuCu/C-1 > RuCu/C-2 ≈RuCu/C-4 > RuCu/C-3 ≈Ru/C, in good agreement with the variation of the Ru 3p binding energy in XPS measurements (Table S3, Supporting Information), due to incomplete decomposition of $RuCl_3$ to Ru nanoparticles.

The Cu K-edge XAS profiles are shown in **Figure** 4a,b, where the absorption edge energies of Cu/C, RuCu/C-1, and RuCu/C-3 samples were all close to that of $CuCl_2$, but slightly greater than that of CuO and markedly higher than that of Cu foil, consistent with the formation of $CuCl_x$ residues in the samples. This can also be manifested in the pre-edge absorption peak, which appeared at 8986.90 eV for Cu/C, RuCu/C-1 and RuCu/C-3, very consistent with that of $CuCl_2$, but markedly different at 8980.88 eV for Cu foil and 8985.17 eV for CuO. The pre-edge shape depends on the number of the *d*-shell electrons and the intensity is proportional to the amount of 3*d*-4p hybridization, where the energy position can reflect the metal oxidation state.[57] Thus, the Cu K-edge XANES suggest the chemical configuration of the Cu centers in Cu/C, RuCu/C-1, and RuCu/C-3 were similar to that of $CuCl_2$, and no metallic Cu or CuO was formed during MIH treatment, in good agreement with the results obtained from the above TEM and XPS measurements.

The corresponding Fourier-transformed extended X-ray absorption fine structures (FT-EXAFS) of the Ru K-edge profiles are shown in Figure 3c. All samples in the series can be seen to exhibit three major peaks at 1.53, 1.84, and 2.44 Å that can be assigned to the Ru–C/O, Ru—Cl, and Ru—Ru bond, respectively, in comparison to the results of Ru foil, $RuCl_3$, and RuO_2.[28] Similarly, the FT-EXAFS of the Cu K edge in Figure 4c exhibit two peaks at 1.50 and 1.91 Å, consistent with those of $CuCl_2$, but markedly different from those of Cu foil and CuO. In fact, the Cu—Cu bond at 2.20 Å was absent in all samples, consistent with the TEM and XPS results that no metallic Cu was found.[58–60]

As described in the experiment section, the EXAFS data were then fitted by using the crystal structure as determined by XRD measurements (Figures S11 and S12, Supporting Information), and the fitting results were listed in Tables S5 and S6 (Supporting Information) (three-peak fittings for Ru and two-peak fittings for Cu). From Table S5 (Supporting Information), it can be seen that the Ru K edge of the sample series exhibited a similar structure of

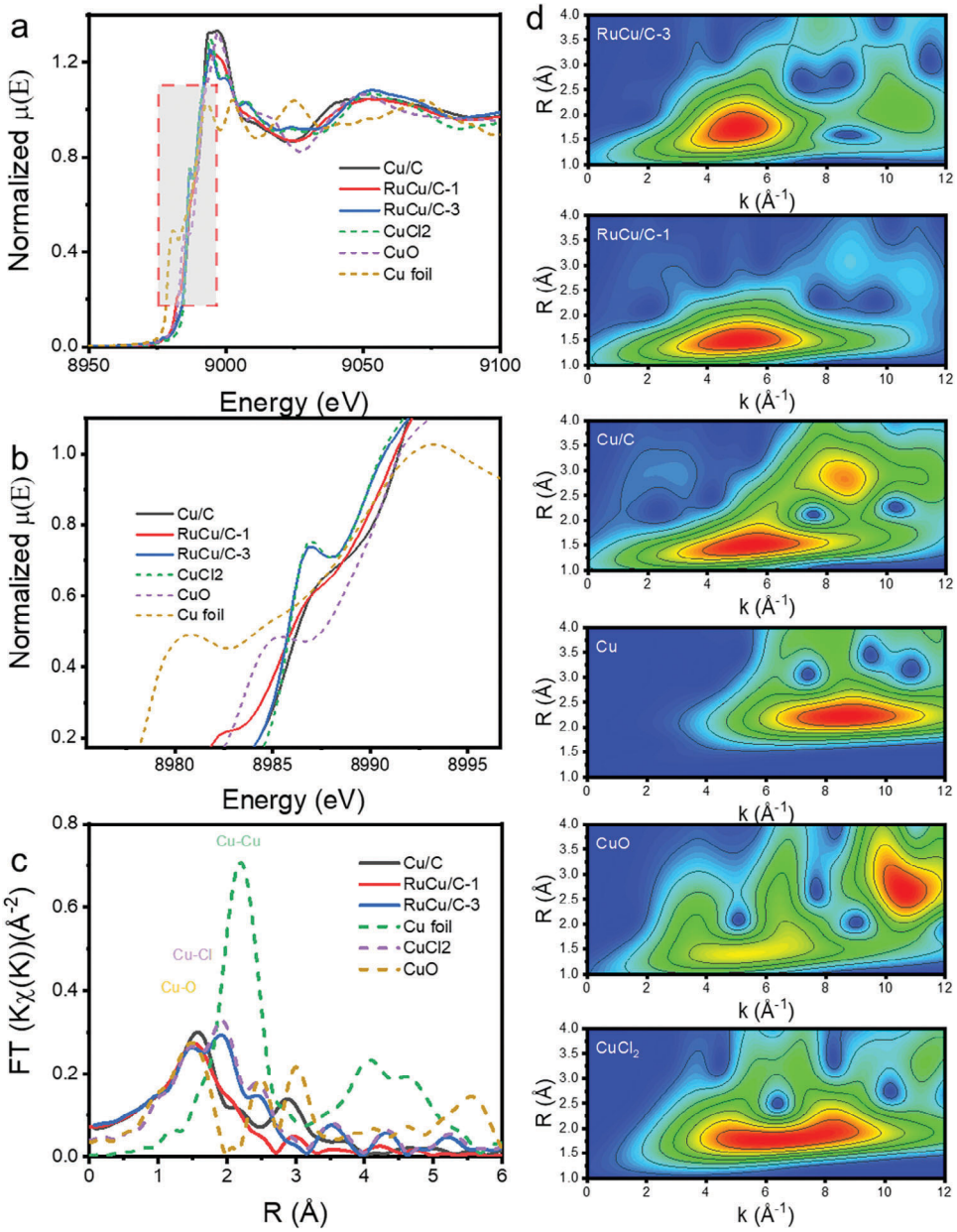

Figure 4. a) X-ray absorption near-edge spectra (XANES) of Cu K, b) zoom-in of the red box in panel (a), c) the corresponding Fourier transformed extended X-ray absorption spectra (FT-EXAFS) of RuCu/C-3, RuCu/C-1, and Cu/C and d) EXAFS wavelet transform analysis ($\kappa = 5$, $\sigma = 1$).

Ru–C/O, Ru–Cl, and metallic Ru–Ru, with a corresponding bond length of 1.98, 2.36, and 2.71 Å, in good agreement with those of the Ru foil, RuO_2 and $RuCl_3$. Yet, the coordination numbers (CN) were markedly lower. For instance, RuCu/C-3 exhibited a CN of 2.37 for Ru-C/O, 2.18 for Ru–Cl, and 1.22 for Ru–Ru, in sharp contrast to 6.00 for RuO_2, 6.00 for $RuCl_3$, and 12.00 for Ru foil. For the fitting results of the Cu K edge data (Table S6, Supporting Information), one can see that the samples also possess a similar structure of Cu–C/O and Cu–Cl, with a bond length of 1.95 and 2.28 Å, respectively, consistent with those from CuO (1.92 Å) and $CuCl_2$ (2.28 Å), but the CN were again markedly lower. For instance, RuCu/C-3 exhibited a CN of 1.06 for Cu–C/O and 3.80 for Cu–Cl, in contrast to 4.00 for CuO and 4.00 for $CuCl_2$. The low CN can be ascribed to the formation of small clusters weakly bound to the carbon matrix.

The corresponding wavelet-transform (WT) diagrams are shown in Figures 3d and 4d using Fortan with Morlet function.[61–62] To compare the atomic configuration, all samples were analyzed using the same parameters of $\kappa = 5$ and $\sigma = 1$. From the WT-EXAFS of the Ru K-edge spectra in Figure 3d, two major peaks can be identified in the contour maps of all samples. The peaks at (4.6 $Å^{-1}$, 1.5 Å) and (10.4 $Å^{-1}$, 1.9 Å) can be assigned to the first-shell Ru—C/O bond and the second-shell Ru—Cl bond, respectively, while the shoulder at (8 $Å^{-1}$, 2.5 Å) can be identified as the metal Ru—Ru bond.[63–64] These results are consistent with the XPS data, where both metallic Ru nanoparticles and Ru–Cl

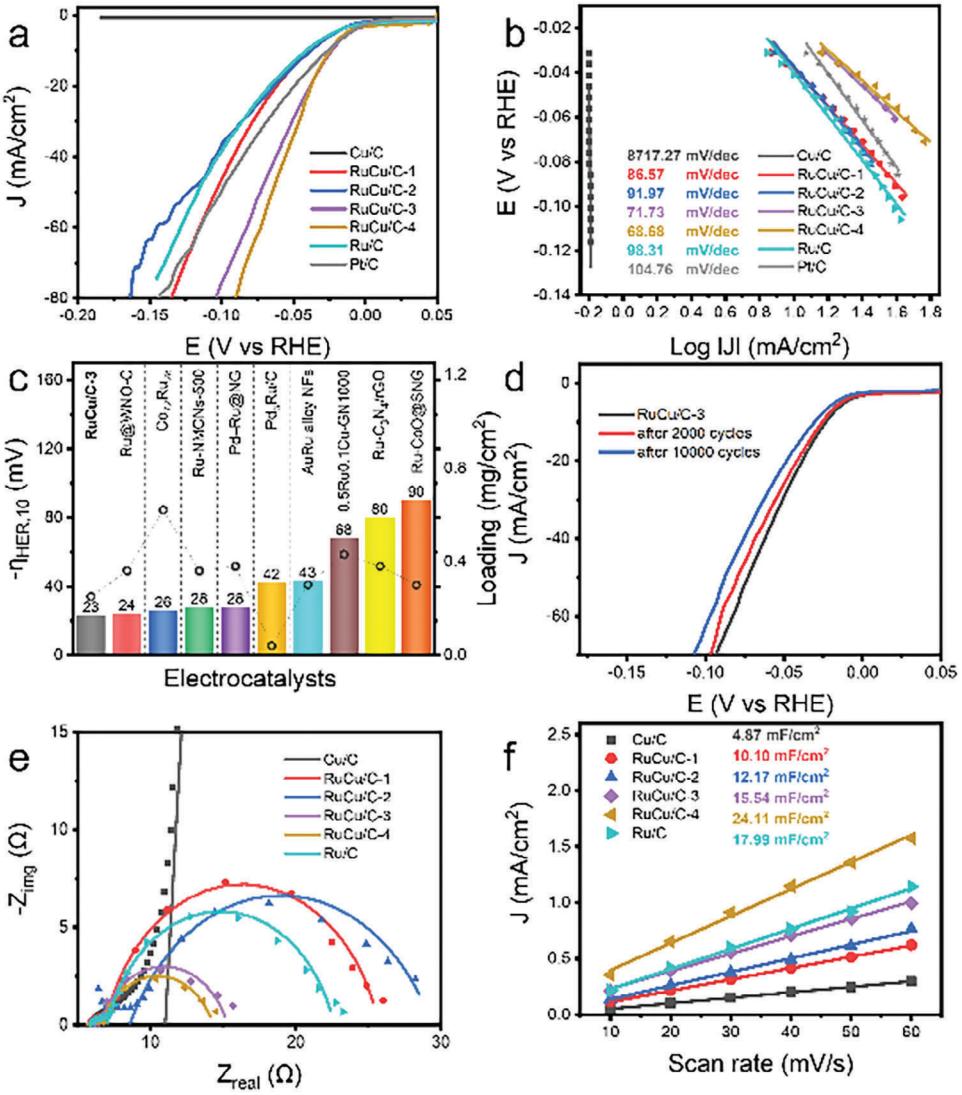

Figure 5. a) HER polarization curves at the rotation rate of 1600 rpm with 100% iR correction and b) the corresponding Tafel plots of the sample series in 1 M KOH. c) Comparison of $\eta_{HER,10}$ between RuCu/C-3 and relevant Ru-based electrocatalysts in recent literature (Table S7, Supporting Information), where the columns represent $\eta_{OER,10}$ (left y-axis), and dotted line represents mass loading (right y-axis). d) HER polarization curves of RuCu/C-3 before and after 2000 and 10000 CV cycles. e) Nyquist plots at −50 mV (symbols are the experimental data and solid lines are the fitting results with the CPE model in Figure S13d (Supporting Information) inset), and (f) variation of the double-layer charging currents with potential scan rates of the sample series in 1 M KOH.

residues were identified. The WT-EXAFS of the Cu K-edge spectra is shown in Figure 4d, where only the first shell Cu—Cl bond at (4.6 $Å^{-1}$, 1.5 Å) can be identified for all samples, and no metallic Cu peak at R = 2.5 Å can be found.

In the above fittings, the metal-C/O paths are indistinguishable. Yet XPS measurements showed the absence of metal-O species in the samples (Figure 2c). Thus, these results further confirmed the formation of carbon-supported Ru nanoparticles decorated with metal-Cl residues and the nanoparticles were dispersed onto a $CuCl_x$ matrix, as suggested by the above TEM and spectroscopic measurements. Additionally, no Ru–Cu path could be resolved, likely due to the low number of interfacial contacts as compared to the bulk phases. Such unique structural characteristics of the RuCu/C nanocomposites, in sharp contrast to the (metallic) ruthenium–copper alloys reported previously,[30–33] led to remarkable bifunctional electrocatalytic activity toward both HER and OER, as detailed below.

2.2. Electrocatalytic Activity

Electrochemical measurements were then conducted to evaluate and compare the electrocatalytic activity of the sample series in both acidic and alkaline media. **Figure** 5a shows the HER polarization curves in 1 M KOH, where one can see that the RuCu/C-3 samples needed only an overpotential ($\eta_{HER,10}$) of −23 mV to achieve the current density at 10 mA cm^{-2}, in comparison to −25 mV for RuCu/C-4, −38 mV for RuCu/C-2, −39 mV for

RuCu/C-1, and −41 mV for Ru/C. Note that both RuCu/C-3 and RuCu/C-4 even outperformed Pt/C (−39 mV), whereas Cu/C exhibited only minimal electrocatalytic activity. This suggests that the HER activity was primarily driven by (metallic) Ru nanoparticles, which were markedly enhanced by metal-Cl residues.[28] The corresponding Tafel plots are depicted in Figure 5b, where the Tafel slope can be found to be very close for RuCu/C-3 (71.73 mV dec^{-1}) and RuCu/C-4 (68.68 mV dec^{-1}), both drastically lower than others in the series, Pt/C (104.76 mV dec^{-1}), RuCu/C-2 (91.97 mV dec^{-1}), RuCu/C-1 (86.57 mV dec^{-1}), and Ru/C (98.31 mV dec^{-1}), suggesting enhanced HER kinetics.[28] The fact that the Tafel slopes were all higher than 40 mV dec^{-1} and exhibited only a relatively small variation among the samples suggests that HER mostly followed the Heyrovsky–Volmer pathway.[65] Notably, the performance of RuCu/C-3 even surpassed those of relevant Ru-based catalysts reported recently in the literature (Figure 5c; Table S7, Supporting Information). These suggest that RuCu/C-3 stood out as the best HER catalyst among the series.

The RuCu/C-3 also exhibited considerable HER performance in acidic media, although subpar as compared to commercial Pt/C.[21] From the polarization curves in Figure S13a (Supporting Information), one can see that the HER activity decreased in order of RuCu/C-3 ($\eta_{HER,10}$ = −92 mV) > RuCu/C-4 (−101 mV) > Ru/C (−110 mV) > RuCu/C-2 (−119 mV) > RuCu/C-1 (−124 mV), with the respective Tafel slope of 72.5, 78.5, 73.8, 78.9, and 79.1 mV dec^{-1} (Figure S13b, Supporting Information).

Moreover, RuCu/C-3 exhibited outstanding durability in both alkaline and acidic media. From Figure 5d, the $\eta_{HER,10}$ can be seen to remain almost unchanged after 2000 potential cycles in 1 M KOH, and shifted negatively by only 8 mV after 10 000 cycles (to −31 mV). In 0.5 M H_2SO_4, the $\eta_{HER,10}$ decayed by only 13 mV after 10 000 potential cycles (Figure S13c, Supporting Information).

Consistent results were obtained from electrochemical impedance spectroscopy (EIS) measurements. The Nyquist plots are shown in Figure 5e and Figure S13d (Supporting Information), where the charge-transfer resistance (R_{ct}) for the sample series was evaluated and compared by fitting the data with the equivalent circuit shown in Figure S13d (Supporting Information) inset. From Table S8 (Supporting Information), one can see that at the overpotential of −50 mV, R_{ct} was the lowest for RuCu/C-4 (7.7 Ω) and RuCu/C-3 (8.8 Ω) in 1 M KOH, in comparison to RuCu/C-2 (20.8 Ω), RuCu/C-1 (18.9 Ω), Ru/C (15.6 Ω) and Cu/C (21 940 Ω). A similar trend can be found in 0.5 M H_2SO_4.

The double layer capacitance (C_{dl}) was then assessed as a measure of the electrochemically active surface area (ECSA) and hence the accessibility of the electrocatalytic active sites by voltametric measurements in the non-faradaic region, which was estimated to be 4.87 mF cm^{-2} for Cu/C, 10.10 mF cm^{-2} for RuCu/C-1, 12.17 mF cm^{-2} for RuCu/C-2, 15.54 mF cm^{-2} for RuCu/C-3, 24.11 mF cm^{-2} for RuCu/C-4, and 17.99 mF cm^{-2} for Ru/C (Figure 5f). The fact that the RuCu/C-3 sample did not possess the largest ECSA among the series suggests that its highest HER activity was due to the intrinsic property rather than the geometric effect.

Notably, the RuCu/C samples also exhibited apparent OER activity. The polarization curves in alkaline media are shown in Figure 6a. RuCu/C-3 can be seen to exhibit a low overpotential ($\eta_{OER,10}$) of +270 mV to reach 10 mA cm^{-2}, in comparison to RuCu/C-4 (+410 mV), RuCu/C-2 (+420 mV), RuCu/C-1 (+430 mV), Ru/C (over +500 mV), and Cu/C (over +500 mV). In fact, the performance was even better than that of commercial 20% RuO_2/C ($\eta_{OER,10}$ = +320 mV). The corresponding Tafel plots are shown in Figure 6b. Among the sample series, RuCu/C-3 featured a lowest Tafel slope of 71.75 mV dec^{-1}, in comparison to Cu/C (181.34 mV dec^{-1}), RuCu/C-1 (101.46 mV dec^{-1}), RuCu/C-2 (92.52 mV dec^{-1}), RuCu/C-4 (87.89 mV dec^{-1}), and Ru/C (120.91 mV dec^{-1}). This suggests that the RuCu/C-3 possessed the most facile electron-transfer kinetics in OER among the sample series and was competitive to commercial RuO_2/C (69.77 mV dec^{-1}). In fact, from Figure S14 and Table S9 (Supporting Information), one can see that the $\eta_{OER,10}$ of RuCu/C-3 was highly competitive to those of relevant Ru-based catalysts reported in the literature even at a relatively low mass loading.

RuCu/C-3 also exhibited good durability toward OER (Figure 6c). After 2000 CV cycles between +1.15 and +1.60 V, the electrode potential at 10 mA cm^{-2} shifted positively by only 150 mV from +1.50 to +1.65 V. In fact, chronopotentiometric tests also confirmed good durability of RuCu/C-3 for HER (Figure S15, Supporting Information) and OER (Figure S16, Supporting Information). Nevertheless, RuCu/C-3 showed only a minimal OER activity in acid (0.5 M H_2SO_4) and cannot reach 10 mA cm^{-2} even at +1.90 V.[66]

Although the HER activity in alkaline media was close for RuCu/C-3 and RuCu/C-4, RuCu/C-3 exhibited the best activity in acidic HER and alkaline OER among the series. Therefore, RuCu/C-3 was exploited as the bifunctional catalyst for overall water splitting in 1 M KOH at the same loading of 1 mg cm^{-2} on carbon paper. From the current–voltage profiles in Figure 6d (solid line), one can see that RuCu/C-3 needed a voltage (E_{10}) of only 1.53 V to produce a current density of 10 mA cm^{-2}, which was 60 mV lower than that with a mixture of commercial 20% Pt/C and RuO_2/C (1.59 V). RuCu/C-3 also displayed excellent durability in electrochemical water splitting. As shown in Figure 6d inset, at the applied voltage of 1.54 V, the current remained markedly greater than that with Pt/C+RuO_2/C during continuous operation for 10 h. The current–voltage profiles after 10 h in Figure 6d (dash line) show the RuCu/C-3 has a small decay of E_{10} by only 30 mV to 1.56 V. Furthermore, the amounts of H_2 and O_2 gases generated were quantified by water displacement tests (Figure S17, Supporting Information), which featured a volume ratio of 2:1, consistent with the stoichiometric ratio of H_2O. From these, the Faradaic efficiency for hydrogen production was estimated to be ≈95%. These results demonstrate that RuCu/C-3 is a viable bifunctional electrocatalyst for electrochemical water splitting.

2.3. Mechanistic Study

In situ XAS measurements were then carried out with the RuCu/C-3 sample in 1 M KOH to further unravel the mechanistic insights into the HER and OER activity. The electrochemical cell is shown in Figure S18 (Supporting Information). A wide range of potentials were applied for HER and OER, and data were acquired at each potential by holding the potential for 1 h. The

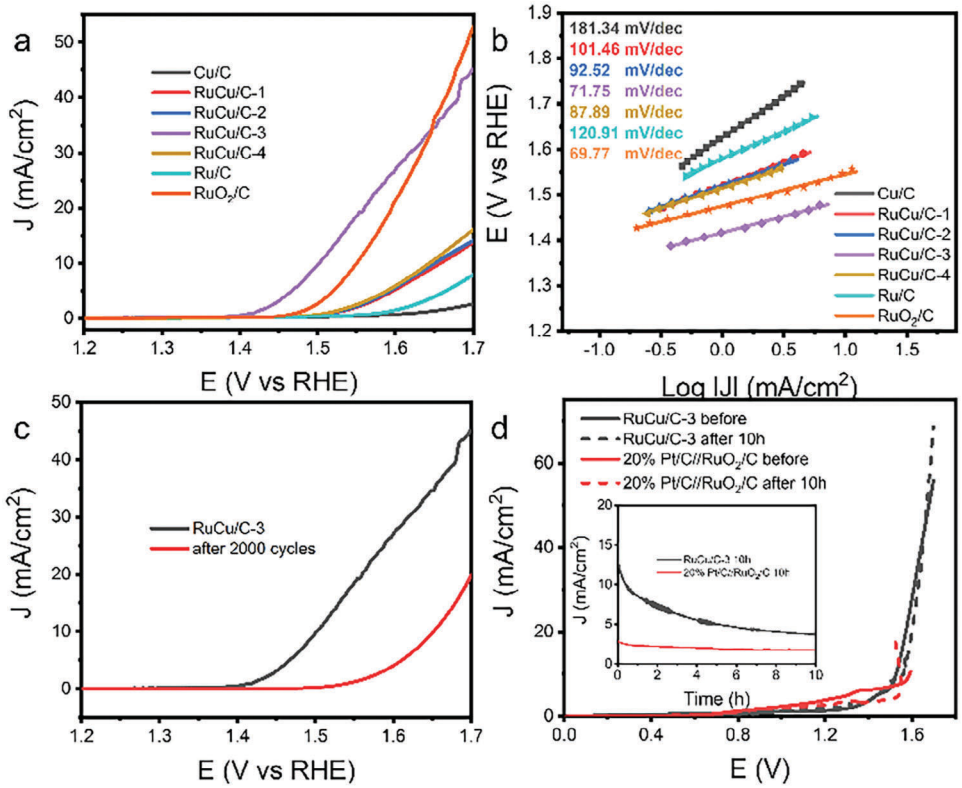

Figure 6. a) OER polarization curves at the rotation rate of 1600 rpm and with 100% iR correction, b) and corresponding Tafel plots of the sample series in 1 M KOH. c) Stability tests of RuCu/C-3 before and after 2000 CV cycles in 1 M KOH. d) Current-potential profiles for full water splitting of RuCu/C-3 and commercial benchmark before and after 10 h stability tests in alkaline media in a two-electrode system. Inset to panel (d) is the corresponding chronoamperometric profiles at the applied voltage of 1.54 V.

Ru K-edge XANES profiles of RuCu/C-3 during HER are shown in **Figure** 7a, where one can see that as the electrode potential was increasingly negative (up to −200 mV), the absorption edge shifted to a lower energy, suggesting electron enrichment of the Ru sites during HER. In the corresponding FT-EXAFS profiles in Figure 7b, the Ru-C/O peak (≈1.5 Å) can be seen to diminish in intensity, and concurrently, that of the metallic Ru—Ru bond (≈2.4 Å) became intensified, with increasingly negative electrode potentials, suggesting that Ru-C/O species was gradually converted into metallic Ru (Figure S19, Supporting Information), and the enrichment of metallic Ru species led to the remarkable HER activity.

The in situ profiles of the Ru K edge during OER are shown in Figure 7c, where the absorption edge can be seen to shift to a higher energy with the application of an increasingly positive potential from +1.2 to +1.8 V. This suggests a higher valence state of Ru in RuCu/C-3 with increasing electrode potential. Additionally, a pre-edge feature emerged at 22 118 eV from the electrode potential of +1.2 to +1.6 V and diminished at +1.8 V. The pre-edge feature is attributed to the formally electric dipole forbidden Ru 4d ← 1s transitions, where the intensity was dependent on the ligand environment and symmetry of the metal center. Ru 5p – 4d mixing breaks centrosymmetric, introducing electric dipole character and causing a change in the pre-edge intensity.[67] Thus, the diminishment of this transition at high overpotentials can be ascribed to the depletion of the valence electrons (i.e., oxidation of Ru and Ru–Cl to RuO_x). Indeed, the corresponding FT-EXAFS curves in Figure 7d and Figure S20 (Supporting Information) can be seen to become increasingly similar to that of RuO_2 with increasing electrode potential, consistent with the Ru Pourbiax diagram.[68] Note that for samples that were prepared at higher induction currents (e.g., 300–600 A), crystalline Ru nanoparticles became the dominant components and no obvious OER activity was observed.[28] This suggests that the high OER activity of RuCu/C-3 was likely due to the Ru–Cl residues that were readily converted to RuO_x at high electrode potentials. That is, it is the dual structure of Ru nanoparticles and Ru–Cl residues in RuCu/C that gave rise to the bifunctional performance toward HER and OER.

The samples were then collected for further structural characterization. In TEM measurements, the lattice fringes of hcp Ru remained well-defined after HER tests, with an interplanar spacing of 0.236, 0.219, and 0.204 nm that can be assigned to the (100), (002), and (101) planes of hcp Ru, respectively (Figure S21, Supporting Information); whereas after OER tests, only the lattice fringes of carbon black can be resolved, with no Ru or RuO_x crystal lattices (Figure S22, Supporting Information), suggesting that at high potentials, the Ru component was transformed into a largely amorphous structure.

The corresponding XPS spectra are shown in Figure S23 (Supporting Information). From Tables S10 and S11 (Supporting Information), one can see that the relative content of metallic Ru

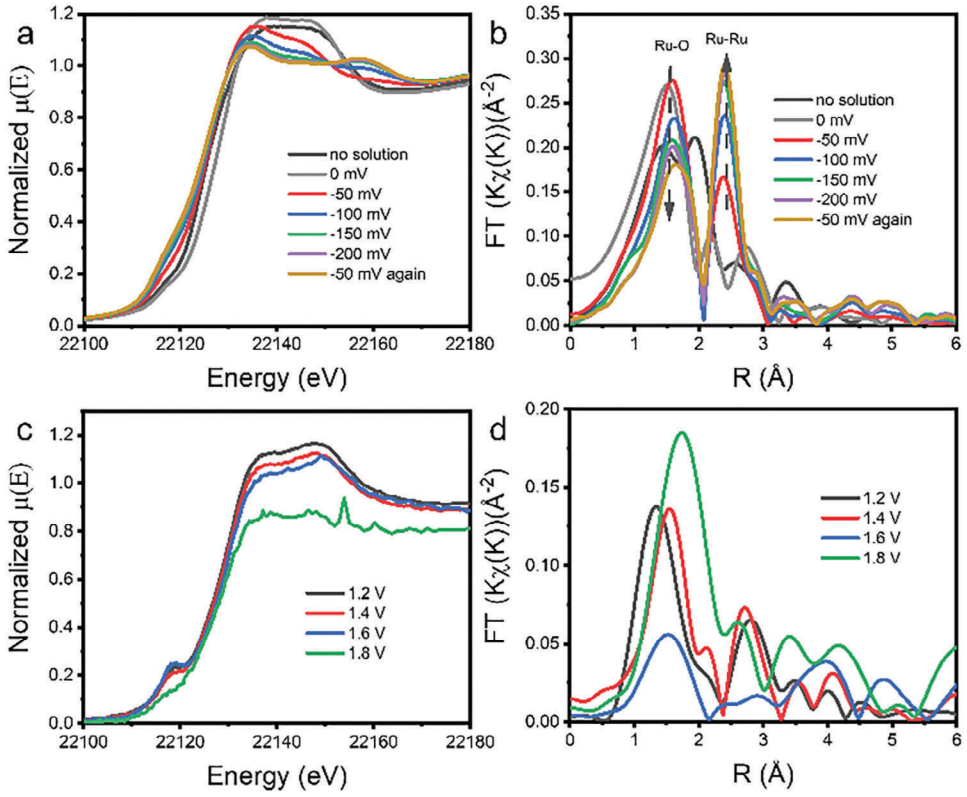

Figure 7. In situ XAS measurements of RuCu/C-3 in 1 M KOH. a) Ru K-edge XANES at different potentials for HER, and b) the corresponding EXAFS curves. c) Ru K-edge XANES at different potentials for OER, and d) the corresponding EXAFS curves.

was increased after HER but decreased after OER, whereas an opposite trend was observed with the $Ru^{\delta+}$ species (no apparent variation with the Cu 2p profile), consistent with the structural dynamics observed in the above in situ XAS studies. Notably, after the electrochemical tests in 1 M KOH, a new peak emerged in the O 1s spectra (Figure S23d, Supporting Information) at 530.26 eV after HER and 530.59 eV after OER suggesting the formation of metal hydroxides (M-OH).[69] In addition, the metal-Cl residues remained rather visible, although the content diminished from 1.75% to 0.40% after HER and 0.50% after OER, likely due to reduction/oxidation of the Ru–Cl species to metallic Ru/Ru–O, in good agreement with results from the in situ XAS studies.

Taken together, these results suggest that the HER-active component was metallic Ru, while RuO_x produced at high electrode potentials was responsible for the OER activity, leading to the remarkable bifunctional performance of the sample.

3. Conclusion

In this study, MIH was employed for the rapid synthesis of RuCu/C nanocomposites, where the addition of $CuCl_2$ precursors was found to facilitate the formation of crystalline Ru nanoparticles, in stark contrast to the largely amorphous structure produced without $CuCl_2$, likely due to galvanic charge transfer from the CuCl intermediates. With the Ru nanoparticle surface decorated with Ru–Cl residues, the RuCu/C samples were found to exhibit apparent electrocatalytic activity toward both HER and OER in alkaline media, with the RuCu/C-3 sample being the best among the series ($\eta_{HER,10} = -23$ mV and $\eta_{OER,10} = +270$ mV). This was ascribed to electroreduction of the Ru–Cl residues at low electrode potential to metallic Ru that was responsible for the HER activity, and oxidation to amorphous Ru oxides at high electrode potentials that were known to be active toward OER, as manifested by in situ XAS measurements. Therefore, the RuCu/C-3 could be exploited as bifunctional catalysts for electrochemical water splitting, needing a potential of only 1.53 eV to produce a current density of 10 mA cm^{-2}, 60 mV lower than that (1.59 V) for a mixture of commercial Pt/C and RuO_2. Results from this study highlight the significance of MIH in the ultrafast synthesis of high-performance bifunctional electrocatalysts.

4. Experimental Section

Chemicals: Ruthenium(III) chloride hydrate ($RuCl_3 \cdot xH_2O$, 35–40%, ACROS Organic), copper(II) chloride ($CuCl_2$, 99%, Aldrich), carbon black (Vulcan XC 72R, Fuel Cell Store), ethanol anhydrous (Fisher Chemicals), acetone (Fisher Chemicals), potassium hydroxide (KOH, 99%, Acros), and sulfuric acid (H_2SO_4, 98%, Fisher Chemicals) were used as received without any further treatment. Water was purified with a Barnstead Nanopure Waster System (resistivity 18.2 MΩ cm).

Sample Preparation: The RuCu/C nanocomposites were synthesized using the MIH set up in Scheme 1. In a typical reaction, 40 mg of carbon black was dispersed into 4 mL of Nanopure water in a 20 mL vial under sonication for 30 min, into which were then added x mL of 0.1 M $RuCl_3$ and y mL of 0.1 M $CuCl_2$ solutions (with x + y = 1 mL, i.e., a total metal feed of 0.1 mmol). After the solution was fully mixed with the

carbon black, the vial was immersed into an acetone-dry ice solution and the solvents were removed by freeze-drying overnight. The obtained black powders were evenly loaded onto a 2.5 cm × 2.5 cm × 0.2 mm iron sheet covered with same-size graphite paper (0.01 mm thick, to avoid direct contact of the precursors with the iron sheets for minimal contamination). The loaded sheets were placed on a fire brick in a quartz tube sealed with a rubber lid, which was purged with high-purity argon gas for 15 min before being inserted into a four-turn induction coil (5 cm in diameter) for MIH treatment at the induction current of 200 A for 10 s. The iron sheet was rapidly heated up to ≈600 °C.[27] After cooling down to room temperature, the obtained sample was washed with H_2O and ethanol 5 times to remove excessive metal salts until the supernatant was colorless and denoted as RuCu/C-1, RuCu/C-2, RuCu/C-3, and RuCu/C-4 in the order of increasing feed ratio of $RuCl_3$ versus $CuCl_2$ at x:y = 1:4, 1:2, 2:1, and 4:1, respectively.

For comparison, samples containing only a single metal precursor were synthesized in the same manner and referred to as Ru/C and Cu/C, respectively.

Characterization: TEM studies were carried out with an FEI Tecni G2 operated at 200 kV. EDS-based elemental mapping analyses were conducted with a Talos F200C G2 TEM instrument as well as with a Thermo Fisher Scientific Apreo S LoVac scanning electron microscope. ICP-OES measurements were carried out with an iCap 7400 instrument. XPS measurements were performed with a Thermo Scientific K_α spectrometer. XRD patterns were acquired with a Bruker D8 Advance diffractometer with Cu K_α radiation ($\lambda = 0.15418$ nm). Ex situ XAS measurements were conducted at the temperature of 10 K using an Oxford liquid helium cryostat at beamline 4–1 of the Stanford Synchrotron Radiation Light source, and in situ XAS data were collected at room temperature in a self-design cell. The obtained XAS data were reduced, fitted, and analyzed with the RSXAP software.[70] The Fourier Transform range was 3.5–12.5 for both Ru K and Cu K edges, while the fit range was 1.1–2.9 for Ru K edge and 1.1–2.5 for Cu K edge. The theoretical functions for each pair (Ru-C/O, Ru–Cl, Ru–Ru, Cu–C/O, and Cu–Cl) were calculated by WebAtoms.[71]

Electrochemistry: Electrochemical tests were conducted with a CHI 700E electrochemical workstation in a typical three-electrode setup. The working electrode was a glassy carbon rotating disk electrode (RDE) with a surface area of 0.196 cm^2, and a graphite rod was used as the counter electrode. Ag/AgCl and Hg/HgO were used as the reference electrodes for acidic and alkaline media, respectively. For ink preparation, 5 mg of the catalysts obtained above were mixed with 200 µL of H_2O, 790 µL of ethanol, and 10 µL of Nafion under sonication for 30 min in an ice bath. The ink (10 µL) and (5 µL) 20% Nafion/IPA solution (corresponding to a catalyst mass loading of 0.25 mg cm^{-2}) was evenly dropcast onto the RDE surface and dried in air. EIS tests were conducted with a Gamry Reference 600 instrument.

Full water splitting tests were performed in a two-electrode setup.[72] Experimentally, graphite paper was thermally treated in air at 500 °C for 1 h. Two 1 cm × 2 cm pieces were cut for the anode and cathode. The catalyst ink (100 mL) (3 mg of catalysts, 60 µL of H_2O, 230 µL of ethanol, and 10 µL of Nafion solution) was loaded on a 1 cm × 1 cm area at a mass loading of 1 mg cm^{-2}. All electrochemical tests were repeated at least three times.

Two pieces of J-shaped carbon paper were used as electrodes for the water displacement measurements in full water splitting in 1 M KOH. Experimentally, 0.5 mg of RuCu/C-3 nanocomposites was loaded on the carbon paper in an area of 1 cm ×1 cm, which was then inserted to the test tubes that was filled with the electrolyte solution. A constant current of 0.5 A was then applied for 20 min, and gases were collected in the two test tubes via the water displacement method.[73]

Supporting Information

Supporting Information is available from the Wiley Online Library or from the author.

Acknowledgements

This work was supported by grants from the National Science Foundation (CHE-1900235 and CHE-2003685). TEM and XPS work was carried out as part of a user project at the National Center for Electron Microscopy and Molecular Foundry, Lawrence Berkeley National Laboratory, which was supported by the US Department of Energy under contract No. DE-AC02-05CH11231. The XAS experiments were performed at the Stanford Synchrotron Radiation Lightsource (SSRL), which is also supported by the US Department of Energy under contract No. DE-AC02-76SF00515. The authors acknowledge Mr. J. Barnett for the assistance in XRD sample preparation and data acquisition and the X-ray Facility at the University of California Santa Cruz for the use of the Rigaku Smartlab Diffractometer, funded by the National Science Foundation (MRI-1126845).

Conflict of Interest

The authors declare no conflict of interest.

Data Availability Statement

The data that support the findings of this study are available from the corresponding author upon reasonable request.

Keywords

bifunctional catalyst, in situ X-ray absorption spectroscopy, magnetic induction heating, ruthenium/copper nanocomposite, water splitting

Received: June 10, 2024
Revised: July 10, 2024
Published online:

[1] National Academies of Sciences, Engineering, and Medicine, *Accelerating Decarbonization of the U.S. Energy System*, The National Academies Press, Washington, DC **2021**.
[2] F. Dawood, M. Anda, G. M. Shafiullah, *Int. J. Hydrogen Energy* **2020**, *45*, 3847.
[3] J. A. Turner, *Science* **2004**, *305*, 972.
[4] A. Haryanto, S. Fernando, N. Murali, S. Adhikari, *Energy Fuels* **2005**, *19*, 2098.
[5] W. Song, M. Li, C. Wang, X. Lu, *Carbon Energy* **2021**, *3*, 101.
[6] Y. Wang, H. Su, Y. He, L. Li, S. Zhu, H. Shen, P. Xie, X. Fu, G. Zhou, C. Feng, D. Zhao, F. Xiao, X. Zhu, Y. Zeng, M. Shao, S. Chen, G. Wu, J. Zeng, C. Wang, *Chem. Rev.* **2020**, *120*, 12217.
[7] L. Quan, H. Jiang, G. Mei, Y. Sun, B. You, *Chem. Rev.* **2024**, *124*, 3694.
[8] A. Ali, F. Long, P. K. Shen, *Electrochem. Energy Rev.* **2022**, *5*, 1.
[9] Y. Peng, Q. M. Liu, B. Z. Lu, T. He, F. Nichols, X. Hu, T. Huang, G. Huang, L. Guzman, Y. Ping, S. W. Chen, *ACS Catal.* **2021**, *11*, 1179.
[10] N. Jiang, B. You, M. Sheng, Y. Sun, *Angew. Chem. Int. Ed.* **2015**, *54*, 6251.
[11] H. Jin, J. Wang, D. Su, Z. Wei, Z. Pang, Y. Wang, *J. Am. Chem. Soc.* **2015**, *137*, 2688.
[12] T. Yu, Z. Wang, K. Tan, H. He, S. Yin, *Mater. Today Phys.* **2023**, *35*, 101138.
[13] G. Huang, M. Hu, X. Xu, A. A. Alothman, M. S. S. Mushab, S. Ma, P. K. Shen, J. Zhu, Y. Yamauchi, *Small Struct.* **2023**, *4*, 2200235.
[14] X. Wang, G. Huang, Z. Pan, S. Kang, S. Ma, P. K. Shen, J. Zhu, *Chem. Eng. J.* **2022**, *428*, 131190.
[15] B. Lu, L. Guo, F. Wu, Y. Peng, J. E. Lu, T. J. Smart, N. Wang, Y. Z. Finfrock, D. Morris, P. Zhang, N. Li, P. Gao, Y. Ping, S. Chen, *Nat. Commun.* **2019**, *10*, 631.

[16] J. Wang, Z. Wei, S. Mao, H. Li, Y. Wang, *Energy Environ. Sci.* **2018**, *11*, 800.
[17] W. J. Mitchell, J. Xie, T. A. Jachimowski, W. H. Weinberg, *J. Am. Chem. Soc.* **1995**, *117*, 2606.
[18] Z. W. Seh, J. Kibsgaard, C. F. Dickens, I. Chorkendorff, J. K. Nørskov, T. F. Jaramillo, *Science* **2017**, *355*, eaad4998.
[19] Y. Yang, Y. Yu, J. Li, Q. Chen, Y. Du, P. Rao, R. Li, C. Jia, Z. Kang, P. Deng, Y. Shen, X. Tian, *Nanomicro Lett.* **2021**, *13*, 160.
[20] E. Skúlason, V. Tripkovic, M. E. Björketun, S. Gudmundsdóttir, G. Karlberg, J. Rossmeisl, T. Bligaard, H. Jónsson, J. K. Nørskov, *J. Phys. Chem. C* **2010**, *114*, 18182.
[21] N. Wang, S. L. Ning, X. L. Yu, D. Chen, Z. L. Li, J. C. Xu, H. Meng, D. K. Zhao, L. G. Li, Q. M. Liu, B. Z. Lu, S. W. Chen, *Appl. Catal. B* **2022**, *302*, 120838.
[22] M. You, X. Du, X. Hou, Z. Wang, Y. Zhou, H. Ji, L. Zhang, Z. Zhang, S. Yi, D. Chen, *Appl. Catal. B* **2022**, *317*, 121729.
[23] R. Jiang, D. T. Tran, J. Li, D. Chu, *Energy Environ. Mater.* **2019**, *2*, 201.
[24] B. Huang, H. Kobayashi, T. Yamamoto, S. Matsumura, Y. Nishida, K. Sato, K. Nagaoka, S. Kawaguchi, Y. Kubota, H. Kitagawa, *J. Am. Chem. Soc.* **2017**, *139*, 4643.
[25] Q. M. Liu, S. W. Chen, *Trends Chem.* **2022**, *4*, 918.
[26] B. Lu, Q. Liu, C. Wang, Z. Masood, D. J. Morris, F. Nichols, R. Mercado, P. Zhang, Q. Ge, H. L. Xin, S. Chen, *Research* **2022**, 9756983.
[27] Q. Liu, S. McNair, F. Nichols, B. Lu, B. Yu, D. Pan, J. Ko, A. Bhuller, F. Bridges, S. Chen, *Adv. Sens. Energy Mater.* **2023**, *2*, 100046.
[28] Q. M. Liu, B. Z. Lu, F. Nichols, J. Ko, R. Mercado, F. Bridges, S. W. Chen, *Susmat* **2022**, *2*, 335.
[29] Q. M. Liu, F. Nichols, A. Bhuller, K. Singewald, H. L. Kuo, J. Q. Lu, G. L. Millhauser, F. Bridges, Q. F. Ge, S. W. Chen, *Appl. Catal. B* **2024**, *342*, 123399.
[30] D. Cao, J. Wang, H. Xu, D. Cheng, *Small* **2020**, *16*, 2000924.
[31] Q. Wu, M. Luo, J. Han, W. Peng, Y. Zhao, D. Chen, M. Peng, J. Liu, F. M. F. de Groot, Y. Tan, *ACS Energy Lett.* **2020**, *5*, 192.
[32] L. Ji, S. Luo, L. Li, N. Qian, X. Li, J. Li, J. Huang, X. Wu, H. Zhang, D. Yang, *Nanoscale Adv.* **2023**, *5*, 861.
[33] J. Zhang, J. Le, Y. Dong, L. Bu, Y. Zhang, J. Cheng, L. Li, X. Huang, *Sci. China Chem.* **2022**, *65*, 87.
[34] B. Zheng, L. Ma, B. Li, D. Chen, X. Li, J. He, J. Xie, M. Robert, T.-C. Lau, *Catal. Sci. Technol.* **2020**, *10*, 4405.
[35] J. Peng, Y. Chen, K. Wang, Z. Tang, S. Chen, *Int. J. Hydrogen Energy* **2020**, *45*, 18840.
[36] F. Li, G.-F. Han, H.-J. Noh, I. Ahmad, I.-Y. Jeon, J.-B. Baek, *Adv. Mater.* **2018**, *30*, 1803676.
[37] Z. Wang, G. Marin, G. F. Naterer, K. S. Gabriel, *J. Therm. Anal. Calorim.* **2015**, *119*, 815.
[38] A. E. Newkirk, D. W. Mckee, *J. Catal.* **1968**, *11*, 370.
[39] D. R. Lide, *CRC Handbook of Chemistry and Physics: A Ready-Reference Book of Chemical and Physical Data*, 85th ed., CRC Press, Boca Raton, Fla **2004**.
[40] V. Sahu, S. Shekhar, P. Ahuja, G. Gupta, S. Singh, R. Sharma, G. Singh, *RSC Adv.* **2013**, *3*, 3917.
[41] F. Tzorbatzoglou, A. Brouzgou, P. Tsiakaras, *Appl. Catal. B* **2015**, *174*, 203.
[42] F. Gao, Y. Wang, X. Wang, S. Wang, *Adsorption* **2016**, *22*, 1013.
[43] S. Y. Tee, C. J. J. Lee, S. S. Dinachali, S. C. Lai, E. L. Williams, H.-K. Luo, D. Chi, T. S. Andy Hor, M.-Y. Han, *Nanotechnology* **2015**, *26*, 415401.
[44] D. J. Morgan, *Surf. Interface Anal.* **2015**, *47*, 1072.
[45] C. Bock, C. Paquet, M. Couillard, G. A. Botton, B. R. MacDougall, *J. Am. Chem. Soc.* **2004**, *126*, 8028.
[46] J. R. Deka, D. Saikia, K. S. Hsia, H. M. Kao, Y. C. Yang, C. S. Chen, *Catalysts* **2020**, *10*, 267.
[47] Y. M. Zhang, H. X. Jiang, G. M. Li, M. H. Zhang, *RSC Adv.* **2016**, *6*, 16851.
[48] X. Qin, L. Zhang, G.-L. Xu, S. Zhu, Q. Wang, M. Gu, X. Zhang, C. Sun, P. B. Balbuena, K. Amine, M. Shao, *ACS Catal.* **2019**, *9*, 9614.
[49] C. Huang, L. Zheng, W. Feng, A. Guo, X. Gao, Z. Long, X. Qiu, *ACS Sustain. Chem. Eng.* **2020**, *8*, 14030.
[50] D.-J. Li, S. Lei, Y.-Y. Wang, S. Chen, Y. Kang, Z.-G. Gu, J. Zhang, *Dalton Trans.* **2018**, *47*, 5558.
[51] A. I. Aria, P. R. Kidambi, R. S. Weatherup, L. Xiao, J. A. Williams, S. Hofmann, *J. Phys. Chem. C* **2016**, *120*, 2215.
[52] Y. Wang, W. Zhou, R. Jia, Y. Yu, B. Zhang, *Angew. Chem. Int. Ed.* **2020**, *59*, 5350.
[53] J. P. Hofmann, S. Zweidinger, M. Knapp, A. P. Seitsonen, K. Schulte, J. N. Andersen, E. Lundgren, H. Over, *J. Phys. Chem. C* **2010**, *114*, 10901.
[54] A. Lebedeva, B. L. Albuquerque, J. B. Domingos, J.-F. Lamonier, J.-M. Giraudon, P. Lecante, A. Denicourt-Nowicki, A. Roucoux, *Inorg. Chem.* **2019**, *58*, 4141.
[55] A. M. Ruppert, M. Jędrzejczyk, O. Sneka-Płatek, N. Keller, A. S. Dumon, C. Michel, P. Sautet, J. Grams, *Green Chem.* **2016**, *18*, 2014.
[56] Y. Peng, W. Pan, N. Wang, J. E. Lu, S. Chen, *ChemSusChem* **2018**, *11*, 130.
[57] A. A. Guda, S. A. Guda, A. Martini, A. N. Kravtsova, A. Algasov, A. Bugaev, S. P. Kubrin, L. V. Guda, P. Šot, J. A. van Bokhoven, C. Copéret, A. V. Soldatov, *NPJ Comput. Mater.* **2021**, *7*, 203.
[58] I. A. Pankin, A. Martini, K. A. Lomachenko, A. V. Soldatov, S. Bordiga, E. Borfecchia, *Catal. Today* **2020**, *345*, 125.
[59] P. Murria, C. K. Miskin, R. Boyne, L. T. Cain, R. Yerabolu, R. Zhang, E. C. Wegener, J. T. Miller, H. I. Kenttämaa, R. Agrawal, *Inorg. Chem.* **2017**, *56*, 14396.
[60] C. Zou, C. Xi, D. Wu, J. Mao, M. Liu, H. Liu, C. Dong, X.-W. Du, *Small* **2019**, *15*, 1902582.
[61] H. Funke, A. Scheinost, M. Chukalina, *Phys. Rev. B* **2005**, *71*, 094110.
[62] H. Funke, M. Chukalina, A. C. Scheinost, *J. Synchr. Radiat.* **2007**, *14*, 426.
[63] W. Zhu, X. Song, F. Liao, H. Huang, Q. Shao, K. Feng, Y. Zhou, M. Ma, J. Wu, H. Yang, H. Yang, M. Wang, J. Shi, J. Zhong, T. Cheng, M. Shao, Y. Liu, Z. Kang, *Nat. Commun.* **2023**, *14*, 5365.
[64] Y. Sun, S. Mu, Z. Xing, J. Guo, Z. Wu, F. Yu, M. Bai, X. Han, C. Cheng, L. Ye, *Adv. Mater.* **2022**, *34*, 2206208.
[65] N. Mahmood, Y. Yao, J.-W. Zhang, L. Pan, X. Zhang, J.-J. Zou, *Adv. Sci.* **2018**, *5*, 1700464.
[66] D. Cao, X. Huang, H. Zhang, W. Liu, D. Cheng, *Chem. Eng. J.* **2023**, *456*, 141148.
[67] K. Getty, M. U. Delgado-Jaime, P. Kennepohl, *Inorg. Chim. Acta.* **2008**, *361*, 1059.
[68] I. Povar, O. Spinu, *J. Electrochem. Sci. Eng.* **2016**, *6*, 145.
[69] J.-C. Dupin, D. Gonbeau, P. Vinatier, A. Levasseur, *Phys. Chem. Chem. Phys.* **2000**, *2*, 1319.
[70] C. Booth, F. Bridges, *Real Space X-ray Absorption Package (RSXAP)*. **1999**, https://lise.lbl.gov/RSXAP.
[71] B. Ravel, *WebAtoms* **2016**, https://millenia.cars.aps.anl.gov/webatoms.
[72] T. He, Y. Song, Y. Chen, X. Song, B. Lu, Q. Liu, H. Liu, Y. Zhang, X. Ouyang, S. Chen, *Chem. Eng. J.* **2022**, *442*, 136337.
[73] Y. Peng, B. Lu, L. Chen, N. Wang, J. E. Lu, Y. Ping, S. Chen, *J. Mater. Chem. A* **2017**, *5*, 18261.

